Nanoscale

PAPER

View Article Online
View Journal | View Issue

Cite this: *Nanoscale*, 2026, **18**, 5422

Facile phase selective synthesis of α- and β-$AgVO_3$: a comparative study of their structural, morphological and photocatalytic properties

Hassan Esmaili, *[a] Marianela Escobar-Castillo, [a] Astita Dubey, [a] Young Un Jin, [a] Sobhan M. Fathabad, [a] Christoph Ochsendorf,[a] Elnaz Tahavori,[b] Shaista Tahir [a] and Doru. C. Lupascu *[a]

$AgVO_3$ is a low bandgap semiconductor (~2 eV) crystallizing in a metastable (α) phase or a thermodynamically stable (β) phase, each exhibiting distinct properties. Despite their photocatalytic potential, synthesizing phase pure α and β-$AgVO_3$ in a simple, reproducible manner remains a challenge. In this study, facile and repeatable synthesis routes are introduced for both phases. The α phase is obtained *via* a low-temperature precipitation method, while the β-phase is synthesized through a hydrothermal process at 120–160 °C. A comprehensive comparison of the structural, morphological, optical, and photocatalytic properties of both phases is conducted. Both exhibit a monoclinic structure and a rod-like morphology; however, the α phase shows a unique tree-like morphology with nanorod growth on microrods. Differential scanning calorimetry (DSC) analysis on α-$AgVO_3$ over three heating and cooling cycles and high-temperature X-ray diffraction show that the α-to-β phase transition is an irreversible exothermic process occurring between ~200 and 240 °C. The complete electronic band structures of both phases were also determined, with the valence and conduction band positions for the α- and β-phase samples determined to be (1.13, −0.94 eV) and (0.92, −1.08 eV) *versus* NHE, respectively. The unique morphology of α-$AgVO_3$ contributes to its enhanced photocatalytic activity. Interestingly, and in contrast to previous reports favoring the β-phase, the α-phase demonstrates superior photocatalytic efficiency, achieving complete degradation of rhodamine B within 90 minutes, while the β-phase reaches 89% degradation after 180 minutes. This finding challenges the conventional assumption that the β-phase always outperforms the α-phase and suggests that morphology and surface structure can play a more critical role than crystallinity in determining photocatalytic performance.

Received 30th September 2025,
Accepted 23rd January 2026

DOI: 10.1039/d5nr04142b

rsc.li/nanoscale

1. Introduction

Rapid global development has led to serious challenges like scarcity of clean water, driven by pollution from industrialization and urbanization. Organic dyes, as an industrial pollutant from different industries such as leather, paper and textile companies, are often discarded into water resources without further treatment. The amount of allowed dye (*e.g.*, rhodamine B and methylene blue) concentrations discharged into the environment is less than 1 mg L^{-1}, according to the international standard of effluent discharge. The requirement for effective organic dye removal from water resources is thus imminent.[1] Among various methods, advanced oxidation processes, especially photocatalysis using solar energy, are promising for efficiently degrading harmful organic pollutants.[2] During photocatalysis, light energy excites a photocatalyst, generating electron–hole pairs that produce reactive oxygen species (ROS), which break down organic pollutants.[3] Various materials, including metal oxides,[4] metal sulfides,[5] perovskites,[6] and, more recently, metal vanadates,[7] have been proposed as potential candidates.

Metal vanadate photocatalysts show great potential due to their high light absorption, narrow band gap in the visible light range, diverse electronic structures, which enable various photocatalytic applications such as the hydrogen and oxygen evolution (HER and OER) reactions, methane (CH_4) and carbon dioxide (CO_2) reduction, and finally their excellent chemical stability. Different types of metal vanadate semiconductors, including bismuth vanadate ($BiVO_4$),[8] silver vanadate ($AgVO_3$),[9] and indium vanadate ($InVO_4$),[10] have been explored for their photocatalytic applications. Depending on their electronic band structure, these materials have been used in photocatalytic processes such as organic dye

[a]*Institute for Materials Science and Center for Nanointegration Duisburg-Essen (CENIDE), University of Duisburg-Essen, 45141 Essen, Germany. E-mail: hassan.esmaili@stud.uni-due.de, doru.lupascu@uni-due.de*
[b]*Department of Chemistry, Stockholm University, Stockholm, SE-10691, Sweden*

degradation,[11,12] CO_2 reduction,[13,14] and hydrogen production.[15–17]

In recent years, silver-based materials have been developed as highly efficient photocatalysts due to their narrow band gaps, the involvement of highly reactive Ag^+ ions and their fully filled d^{10} orbitals in the energy band structure.[18] The unique hybridization of V 3d, O 2p and Ag 4d orbitals in the valence band results in a narrow band gap, making $AgVO_3$ an ideal candidate for activation under visible light irradiation.[19] $AgVO_3$ typically has a rod-shaped structure with a high surface area and efficient electron–hole separation, both of which enhance its photocatalytic performance.[20–24] One-dimensional (1D) nanomaterials, compared to nanoparticles, offer a larger surface-to-volume ratio and improved charge transfer capabilities.[25] $AgVO_3$ powders have been used in a wide variety of applications, such as photocatalytic degradation of harmful dyes,[26] Li-ion batteries,[27] oxygen evolution reactions (OERs),[9] and photoluminescence[28] and biomedical applications.[29] For instance, $AgVO_3$ nanorods were synthesized using the thermal decomposition method and tested for the degradation of methylene blue (MB) and an industrial effluent. The reported degradation efficiencies were 85% for MB and 95% for the industrial effluent.[26]

Four different crystal structures have been reported for $AgVO_3$, where α-type, γ-type and δ-type are metastable phases, while β-type is the thermodynamically stable phase. The crystal structures of γ- and δ-$AgVO_3$ have not been reported yet. But the crystal structures of α- and β-$AgVO_3$ have been completely determined. The crystal structures of α-$AgVO_3$ and β-$AgVO_3$ were reported to be monoclinic with the $C2/c$ and $C2/m$ space groups, respectively.[28,30] The schematic of the crystal structures is shown in Fig. 1.[2,31–34] It is reported that a phase transition from α to β happens at 200 °C.[35] Various synthesis methods have been employed to directly prepare rod-shaped α- and β-$AgVO_3$ powders, including precipitation, hydrothermal methods, microwave- and ultrasonic-assisted techniques, sol–gel processing, thermal decomposition, microemulsion, and soft chemical *in situ* methods.[36] Each synthesis method offers specific advantages, influencing the material properties. The crystal structure, morphology, crystallinity, particle size, surface termination, and purity of the samples largely depend on the chosen synthesis method.[36]

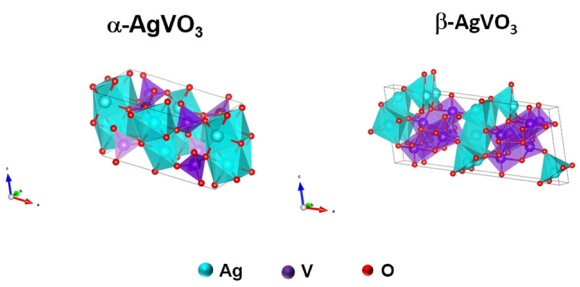

Fig. 1 The crystal structures of α- and β-$AgVO_3$ are shown at the unit-cell level, with polygons highlighting the coordination environments of the central heavy metal atom (cyan for Ag atoms and purple for V atoms) surrounded by its nearest neighbor O atoms. In the case of α-$AgVO_3$, Ag forms a six-fold coordination with O, resulting in an "octahedral" shape, while V forms a four-fold coordination with O, resulting in the "tetrahedral" shape. In β-$AgVO_3$, both Ag and V form a six-fold coordination with O, resulting in the "octahedral" shape. This picture is generated using VESTA using MP-559736 and MP-1178815 from the Materials Project database.

In an initial study by Konta *et al.*,[9] α-$AgVO_3$ and β-$AgVO_3$ were synthesized using precipitation and solid-state methods. It was reported that with an increase in temperature during precipitation from 5 to 25 °C, the α phase changes to the β phase. Also, the β phase can be produced using the solid-state method and calcined at 380 °C for 4 hours, and it was concluded that β-$AgVO_3$ prepared using the solid-state method shows higher activity because of higher crystallinity. In another study by Zeng *et al.*,[35] β-$AgVO_3$ was derived from α-$AgVO_3$ *via* a water evaporation process. NH_4VO_3 and $AgNO_3$ were dissolved in DI water and mixed at 80 °C to form the α phase. Then the prepared α-$AgVO_3$ (orange precipitate) was kept in an oven for 6 h at 100 °C to gradually evolve to the β phase. Also, the structural conversion of Ag nanoparticle-decorated α-$AgVO_3$ to β-$AgVO_3$ by annealing at 475 °C was studied by McNulty *et al.*[37] Furthermore, the possibility of a phase transition during the coprecipitation synthesis of $AgVO_3$ by increasing the temperature from 0 to 75 °C was studied. It was reported that at temperatures higher than 45 °C, the α-to-β phase transition occurred.[28]

Although various synthesis methods have been used for preparing α- and β-$AgVO_3$, there is still a lack of a comprehensive, reliable and reproducible method for preparing pure single phase α and β phases. As previously noted, various methods have been reported for synthesizing the α- and β phases at different temperatures. However, inconsistencies in the literature, such as differing phases reported for the same temperature and synthesis method,[37,38] make it challenging to establish a clear and reliable protocol. Currently, no general and repeatable synthesis method has been reported that provides clear guidance for the preparation of α and β phases and an understanding of the transition of the α to β phase. Therefore, a simple, repeatable and detailed synthesis method for both the α and β phases is needed to show the exact steps for the synthesis of the two phases and their phase transition. In addition to addressing this gap, the present study also aims to evaluate the photocatalytic performance of the two phases to identify which one offers higher efficiency for photocatalytic applications.

Among the commonly used methods, co-precipitation and hydrothermal techniques are widely employed for $AgVO_3$ preparation.[36] It seems that at lower temperatures, the α phase is stable and at higher temperatures, the β phase is stable. In our study, single phase and pure α- and β-$AgVO_3$ were successfully synthesized using precipitation and hydrothermal methods, respectively. Also, the α-to-β phase transition was studied comprehensively using differential scanning calorimetry (DSC) and high temperature X-ray diffraction (HTXRD) techniques to determine the phase transition temperature and the structural change during the phase transition. In addition,

the complete electronic band structures of both α- and β-$AgVO_3$ were experimentally determined. Moreover, a comparative study on the performance of the synthesized α- and β-$AgVO_3$ as photocatalysts in rhodamine B (a harmful dye) degradation was also performed. The effects of different parameters such as the phase, particle size, active surface area, bandgap and surface oxidation states are studied and compared. The results reveal that the synthesis method and $AgVO_3$ particle size have more effects on the photocatalytic activity of $AgVO_3$ powders than their crystal phase.

2. Experimental

2.1. Materials

$NaVO_3$ (99.9%), TiO_2 (commercial P25), and rhodamine B were of analytical grade and purchased from Sigma-Aldrich. $AgNO_3$ (99.9%) was obtained from Carl Roth and used as received without further purification. All aqueous solutions were prepared using ultra-pure de-ionized (DI) water.

2.2. Preparation of $AgVO_3$ – precipitation and hydrothermal methods

$AgNO_3$ and $NaVO_3$ were used as starting materials for the precipitation synthesis of $AgVO_3$. First, 0.61 g of $NaVO_3$ was dissolved in 15 mL of DI water at 70 °C. Once fully dissolved, the solution was maintained at 35 °C (Solution A). Then, separately, 0.85 g of $AgNO_3$ was dissolved in 15 mL of DI water at room temperature (Solution B). Both solutions were stirred vigorously to ensure full dissolution and transparency. Then, Solution B was added dropwise to Solution A using a pipette while maintained at different temperatures (25 °C, 60 °C, 70 °C, and 80 °C). Upon addition, a yellow–orange suspension formed. The mixture was then stirred for 1 h to achieve a homogeneous suspension. The resulting suspension was washed several times with DI water to remove the impurities and then dried naturally at room temperature without additional heating. It is worth noting that exposure to high temperature and drying the sample in an oven were avoided, as they lead to a color change (orange to green) in $AgVO_3$. For the hydrothermal synthesis, the same initial suspension as used in the precipitation method (prepared from the same starting materials) was transferred to a 150 mL Teflon-lined stainless-steel autoclave and maintained at different temperatures (120 °C, 140 °C and 160 °C) for 1 h. The products were washed multiple times with DI water to reach maximum purity and dried naturally at room temperature without heating. The synthesized powders from precipitation and the hydrothermal method are hereafter referred to by their sample codes as shown in Table 1.

Table 1 Sample codes and their corresponding synthesis regime

Synthesis method-temperature (°C)	Code
Precipitation-25	P25
Precipitation-60	P60
Precipitation-70	P70
Precipitation-80	P80
Hydrothermal-120	H120
Hydrothermal-140	H140
Hydrothermal-160	H160

2.3. Characterization

X-ray powder diffraction (XRD) was performed using an Empyrean Series 2 diffractometer (PANalytical) with Cu K_α radiation (λ = 1.54 Å) to analyze the phase composition. The crystallite size and dislocation density of the synthesized materials were estimated using the Williamson–Hall equation.[39] The specific surface area of the as-prepared samples was determined from nitrogen adsorption–desorption isotherms measured at 77 K using a Gemini VII 2390 (version 1.03). The Brunauer–Emmett–Teller (BET) equation was applied to calculate the total surface area. Morphological analysis was conducted using a scanning electron microscope (Philips XL 30 ESEM). The optical properties of the samples were investigated using a UV-visible spectrophotometer (Shimadzu UV-2600). Fourier-transform infrared (FTIR) spectra were recorded in ATR mode using an ALPHA Platinum spectrometer (Bruker). X-ray photoelectron spectroscopy (XPS) and ultraviolet photoelectron spectroscopy (UPS) were employed to analyze the elemental oxidation states and binding energy states (PHI 5000 VersaProbe II). The phase transition behavior and the thermal properties of the α-$AgVO_3$ sample were examined using differential scanning calorimetry (DSC; Caliris 300, Netzsch) with heating and cooling rates of 20 °C min^{-1} each. Atomic force microscopy (AFM) and Kelvin probe force microscopy (KPFM) measurements were performed using an Ntegra scanning probe microscope (NT-MDT, Russia).

2.4. Experimental procedure

2.4.1. Photocatalytic experiments. Rhodamine B (RhB) and methyl orange (MO) were selected as model dyes to probe the photocatalytic performance of the as-synthesized $AgVO_3$ powders under visible light irradiation. The experiments were carried out using a batch photoreactor equipped with a solar-light simulator source (three commercial LED panels, 300 W total, full spectrum) placed around the solution. In a typical process, 50 mL of aqueous suspension was prepared containing 5 mg of $AgVO_3$ powder and 5 mg L^{-1} RhB (or MO). Prior to visible light irradiation, the adsorption–desorption equilibrium was established between the surface of the catalyst and the dye molecules by stirring the solution for 30 min in the dark.

At certain time intervals (5, 10, 30, 60, 90, 120 and 180 min), 1 mL of sample solution was withdrawn, and the centrifuged (30 min, 7500 rpm) supernatant was collected for further analysis.

The degradation of RhB was monitored using a UV-vis spectrophotometer (Shimadzu UV-2600) by tracking the change in its main characteristic absorption peak. Specifically, the degradation process was monitored by the change in the maximum absorbance of the dye at a wavelength of 554 nm

corresponding to the RhB primary peak. According to Beer–Lambert's law, the concentration of a solution is directly proportional to its absorbance.[40] Therefore, the normalized temporal concentration changes (C_t/C_0) of dyes correspond to the normalized maximum absorbance (A_t/A_0). A_0, A_t, and C_0, C_t are the absorbances at the aforementioned maximum peaks and concentrations of dyes when the reaction time was 0 and t, respectively.[41,42]

To investigate the role of reactive oxygen species in the photocatalytic oxidation process, methanol and *p*-benzoquinone were employed as hole and electron scavengers, respectively.[43,44] The experiments followed the same procedure as the standard photocatalytic tests, with the addition of 1 mM each scavenger prior to irradiation.

2.4.2. Kinetic study of photocatalytic dye degradation. Pseudo-first- and pseudo-second-order kinetic models were employed to explain the mechanism of dye degradation in solution and to evaluate the photocatalytic reaction rate. These models are particularly suitable when the kinetic study is based solely on the variation of dye concentration with respect to time. In the present study, the effects of light intensity, photocatalyst dosage, and temperature were assumed to be negligible and were not systematically investigated. Therefore, instead of applying true first- or second-order kinetic models, pseudo-order kinetic models were considered to describe the degradation kinetics. The general form of the pseudo-order kinetics is given in eqn 1:

$$-\frac{dC_t}{dt} = k_n C_p^n \quad (1)$$

where n is the reaction order. It is a real number typically ranging from 0 to 2. However, it is mostly reported as an integer. The integrated form of eqn (1), using $n = 1$ and $n = 2$ yields the general formula for the pseudo-first order (eqn (2)) and pseudo-second order (eqn (3)) kinetics models:

$$\mathrm{Ln}\frac{C_t}{C_0} = -k_1 t \quad (2)$$

$$\frac{1}{C_t} - \frac{1}{C_0} = k_2 t \quad (3)$$

where k_1 and k_2 represent the rate constants for the pseudo-first and pseudo-second order kinetic models, respectively.[45]

3. Results and discussion

Fig. 2 shows the XRD patterns of $AgVO_3$ powders synthesized using $AgNO_3$ and $NaVO_3$ as precursors *via* different synthesis methods and temperatures. At room temperature, only the α phase was formed. The XRD pattern for P25 could be well matched to the α-phase crystal structure of $AgVO_3$ (JCPDS no. 98-005-0645). However, increasing the synthesis temperature in the precipitation method leads to structural changes, indicating the transformation of the α phase. For the samples synthesized using precipitation at elevated temperatures (60 °C, 70 °C, and 80 °C), the crystal structures deviate from the

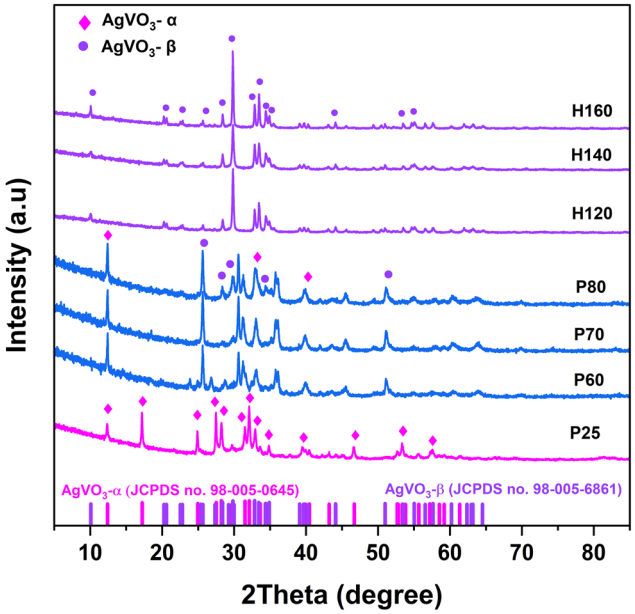

Fig. 2 XRD patterns of all the synthesized samples *via* precipitation and the hydrothermal method.

α-phase. While some peaks, such as those near 12, 31, 37, and 40 degrees, appear in both the room-temperature and higher-temperature samples, several characteristic α-phase peaks (*e.g.*, at 17, 27, and 32 degrees) disappear with increasing temperatures. Additionally, the intensity of the peak at 24 degrees (prominent in P25) decreases at 60 °C and vanishes completely at higher temperatures. These findings contrast with the study by de Menezes *et al.*[46] who reported the formation of β-$AgVO_3$ using the precipitation method at 30 °C, 60 °C, and 90 °C. Another study, by Oliveira *et al.*,[28] reported that α-$AgVO_3$ can be synthesized up to 45 °C, beyond which the β-phase becomes stable. However, in the present study, β-phase formation could not be achieved using the precipitation method even at 60–80 °C. Successful synthesis of the β-phase was achieved using the hydrothermal method. As shown in Fig. 2, all peaks of the hydrothermal samples (H120, H140, H160) match the β-$AgVO_3$ reference pattern (JCPDS no. 98-005-6861). Both α- and β-$AgVO_3$ exhibit monoclinic crystal systems but differ in the space group: the α-phase crystallizes in the $C2/c$ (no. 15) space group, whereas the β-phase adopts $C2/m$ (no. 12) (Table 2). Table 2 summarizes the crystallographic parameters and crystallite sizes of the samples, calculated using Rietveld refinement and the Williamson–Hall equation. Notably, the H160 sample shows the largest average crystallite size (70.79 nm), which is significantly larger than those of the other samples. In addition, an increase in the synthesis temperature leads to a decrease in dislocation density, indicating improved crystallinity.[47] This increase is attributed to enhanced crystal growth at higher synthesis temperatures.[48] The crystal structures and phase purity of the P60, P70, and P80 samples could not be definitively determined. Their XRD patterns show features of α-, β-$AgVO_3$ and other peaks that

Table 2 Crystal structure information of all samples synthesized using precipitation and hydrothermal methods at different temperatures using Rietveld refinement (goodness of fit: 1.35–1.85) and Williamson–Hall equations

Sample	Crystal structure	Space group	a (Å)	b (Å)	c (Å)	α (°)	β (°)	γ (°)	Cell volume (10^{-6} pm^3)	Average crystallite size (nm)	Dislocation density (10^{-4} nm^{-2})
P25	Monoclinic	$C2/c$ (15)	10.43	9.91	5.51	90	99.59	90	561.92	35.08	8.13
H120	Monoclinic	$C2/m$ (12)	18.13	3.58	8.04	90	104.71	90	497.44	60.76	2.71
H140	Monoclinic	$C2/m$ (12)	18.10	3.58	8.03	90	104.48	90	503.84	65.82	2.31
H160	Monoclinic	$C2/m$ (12)	18.11	3.58	8.04	90	104.47	90	504.34	70.79	2.00

cannot be indexed to the known silver vanadate compounds, making it difficult to confirm their phase and whether they are single-phase materials. The β-phase exhibits a smaller unit cell volume compared to the α-phase. As shown in Table 2, the α phase has a calculated cell volume of 562 (10^6 pm^3), while hydrothermal (β) samples show smaller volumes ranging from 497 to 504 (10^6 pm^3).

The morphology and rod width distribution of the α-phase (P25) and β-phase (H120, H140, and H160) samples are illustrated in Fig. 3. All samples exhibit rod-shaped structures with a high degree of agglomeration, which may contribute to reduced surface area. As the synthesis temperature increased, the particle size also increased, indicating continued particle growth. The largest particle size was observed in the H160 sample (average rod-width 82.89 nm), synthesized at the highest temperature, whereas the P25 sample displayed a mixture of microrods and nanorods with comparatively smaller particle sizes (average rod-width 34.89 nm). The β-phase samples show relatively uniform morphologies with rod-widths of 61.03, 69.85, and 82.89 nm for H120, H140 and H160, respectively. The α-phase P25 sample, synthesized at room temperature, exhibits a distinct tree-like structure. In this case, it appears that larger rods initially form and subsequently serve as nucleation sites for the growth of $AgVO_3$ nanorods. As a result, the surfaces of these microrods are densely covered with nanorods having mostly widths between 25 and 50 nm (Fig. 3a and b).

Fig. 4(a) displays the FTIR spectra of samples synthesized using both precipitation and the hydrothermal method. As shown, all samples exhibit absorption peaks below 1500 cm^{-1}. The P25 sample displays five distinct peaks located at 500, 620, 775, 900, and 930 cm^{-1}. In comparison, the hydrothermally synthesized samples (H120, H140, and H160) show three main peaks at 500, 785, and 866 cm^{-1}. The peak observed at 500 cm^{-1} in all samples is attributed to the symmetric stretching vibration of V–O–V bonds.[2,23,49] The peaks at 620, 775 and 785 cm^{-1} correspond to the asymmetric stretching vibration of the VO_3 group.[26] Also, the double bond vibration of V=O appears at higher wavenumbers, at 866 cm^{-1} for the β-phase sample and at 900–930 cm^{-1} for the α-phase samples.[50,51]

Furthermore, Fig. 4(b) shows the FTIR results of the P25 sample before and after the photocatalysis experiment. As illustrated, there is no significant change in the FTIR results before and after photocatalysis and all peaks remain below 1000 cm^{-1}. This indicates the absence of residual organic species after photocatalytic degradation, suggesting that complete degradation of RhB was achieved on the surface of the P25 sample. Only a slight shift in peak position is observed; for example, the peak at 500 cm^{-1} shifts slightly to 495 cm^{-1} after the P25 sample was used for photocatalytic RhB degradation.

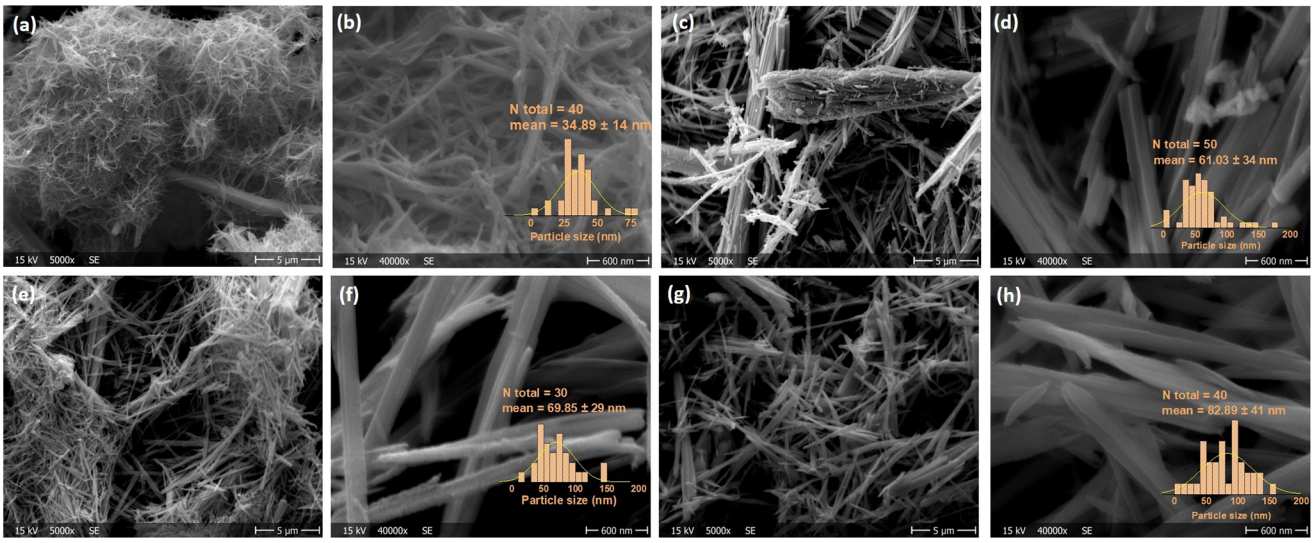

Fig. 3 SEM images of (a, b) P25, (c, d) H120, (e, f) H140, and (g, h) H160. Observe the different scales in both columns.

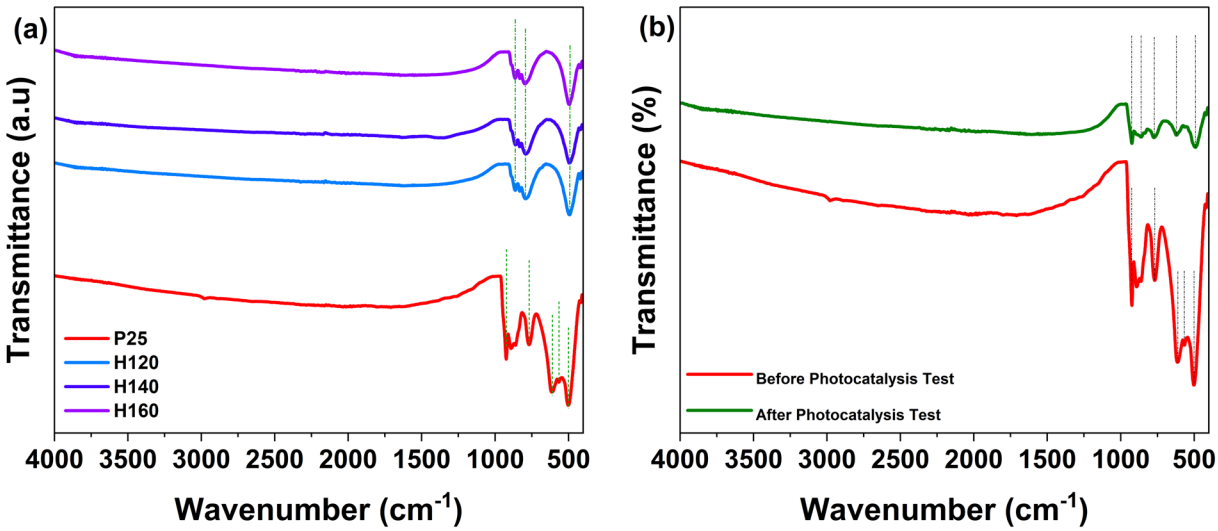

Fig. 4 (a) FTIR spectra of precipitation and hydrothermal synthesized samples P25, H120, H140, and H160 (inset higher magnification); (b) FTIR spectra of the P25 sample before and after the photocatalysis test (inset higher magnification).

To better understand the phase transition from α to β, DSC analysis was conducted on the P25 sample. Fig. 5 shows the DSC results over three heating and cooling cycles between room temperature and 380 °C. An irreversible endothermic peak around 160 °C may be associated with the evaporation and removal of residual solvents trapped within the powder structure. This peak likely does not correspond to a phase transition, as XRD analysis confirms that the α-phase crystal structure remains unchanged at 160 °C (Fig. 5c). In contrast, a prominent irreversible exothermic peak observed between 200 and 240 °C is attributed to the phase transition from α to β-$AgVO_3$. This transition temperature aligns with findings reported in previous research.[35] The phase transition is further supported by XRD and HTXRD analyses. To confirm the DSC results, the P25 sample was heat-treated at 160, 208, 230, and 375 °C in a muffle furnace (Fig. 5c). The XRD patterns show that the sample treated at 160 °C retains the α-phase structure, while those treated at 208 °C, 230 °C, and 375 °C exhibit the β-phase structure.

To observe the phase transformation more precisely and under conditions similar to those of the DSC test (*i.e.*, consistent heating/cooling rates), HTXRD was performed. The HTXRD results clearly indicate the transition from metastable α to thermodynamically stable β at temperatures above 200 °C. As shown in Fig. 5d, the characteristic α-phase peaks at 12.5° and 16° gradually diminish above 200 °C. A minor peak appears at 9° in the HTXRD patterns at 180 °C and 200 °C, indicating the onset of the α-to-β transition. At these temperatures, a mixture of α and β phases is detected, before full conversion to β at 220 °C. After the transition, the β-phase (being thermodynamically stable) remains dominant throughout all three DSC cycles. This is consistent with the irreversible nature of the 200–240 °C exothermic peak. Additionally, a reversible peak observed at 370–375 °C corresponds to the melting point of $AgVO_3$. Further HTXRD analysis over three thermal cycles shows a peak at 345 °C, which is attributed to the recrystallization of molten $AgVO_3$ at high temperature (>370 °C).

From the second segments in both cooling and heating, two reversible peaks can be observed. During cooling cycles (segments 2 and 4), two reversible endothermic peaks appear at approximately 345–350 °C and 180–185 °C. As mentioned above, the peak around 350 °C corresponds to the recrystallization temperatures. The lower-temperature peak at 180–185 °C is less clearly understood. To further investigate, HTXRD was performed under similar cooling and heating rates (Fig. 5e). The HTXRD results show no change at around 180 °C during the first cooling cycle, suggesting that this peak is not related to a phase transition. Similarly, in the heating cycles (segments 3 and 5), two reversible endothermic peaks are detected. The peak above 370 °C corresponds to the melting point of $AgVO_3$. However, the peak at approximately 192 °C remains unclear, as HTXRD shows no detectable structural change at this temperature. Overall, based on the HTXRD results (Fig. 5d and e), it can be concluded that the β-phase is the thermodynamically stable phase of $AgVO_3$ after the first formation at a temperature above 200 °C.

Following structural, morphological, and thermal analyses, optical characterization was carried out for the α- and β-phase samples. The UV-vis DRS spectra of all samples are shown in Fig. 6. All samples exhibit broad visible light absorption, with the H160 sample showing the highest absorption intensity. Table 3 summarizes the absorption edge values for each sample. Overall, the hydrothermally prepared samples demonstrate higher absorption edge values (ranging from 616–628 nm) and a greater proportion of visible light absorption than the samples obtained *via* the precipitation method. Among the samples, P25 has the lowest absorption edge at 602 nm, while H160 shows the highest at 628 nm.

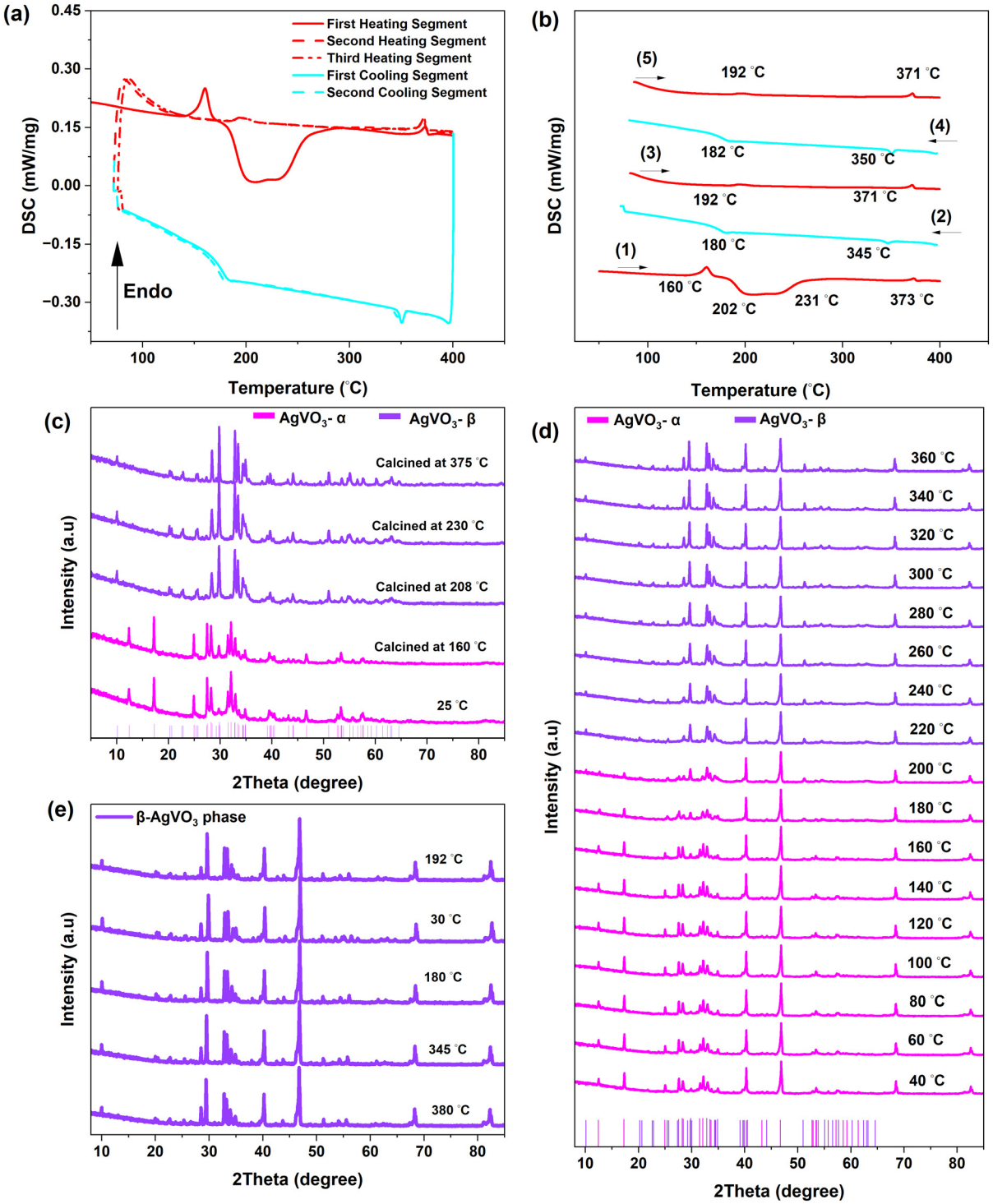

Fig. 5 (a) DSC analysis of sample P25, (b) separated segments of DSC analysis, endo: up (c) XRD results of sample P25 heated to 160, 208, 230 and 375 °C, (d) HTXRD results of sample P25 in the range of 40–360 °C (heating rate 20 °C), and (e) HTXRD of sample P25 at different temperatures.

Furthermore, the bandgap energy (E_g) of the samples was calculated using the Kubelka–Munk equation (eqn (4)):[52]

$$(F(R)h\nu)^{1/n} = A(h\nu - E_g) \quad (4)$$

where $F(R)$, h, ν, A and E_g represent the Kubelka–Munk function, Planck's constant, light frequency, equation constant and bandgap energy, respectively. The exponent n is related to the nature of the electronic transition in the semiconductor; for direct bandgap and indirect bandgap n is equal to $\frac{1}{2}$ and 2, respectively.[53]

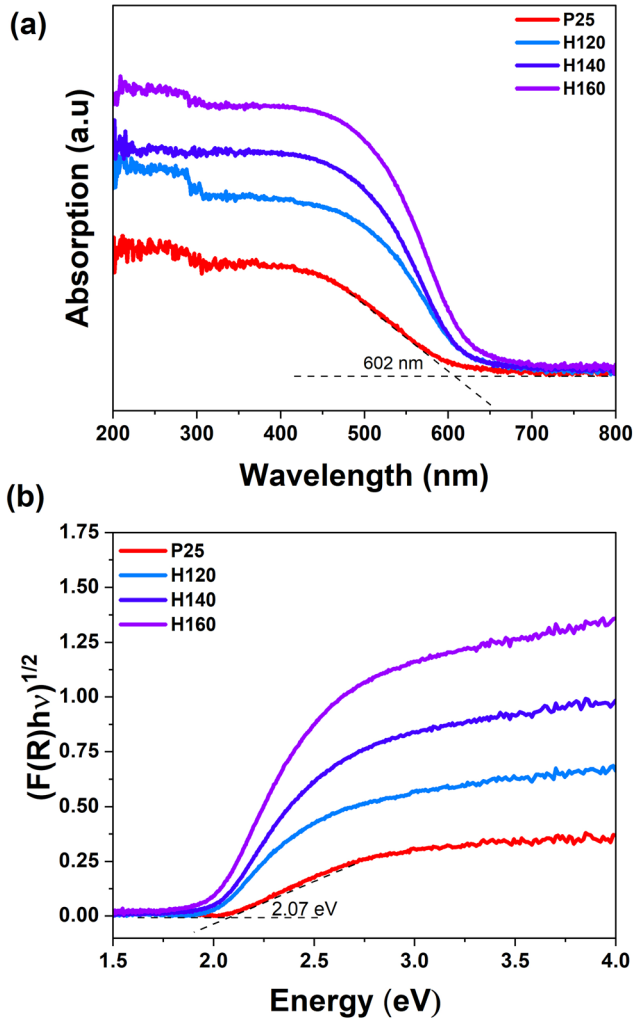

Fig. 6 (a) UV-vis DRS absorption intensity and (b) Tauc plot of the P25, H120, H140, and H160 samples.

Table 3 Calculated bandgap and absorption edge of the samples

Sample	Bandgap (eV)	Absorption edge (nm)
P25	2.07	602
H120	2.00	620
H140	2.00	616
H160	2.01	628

Since $AgVO_3$ is reported to have an indirect bandgap, a value of $n = 2$ was used to calculate the bandgap of all samples.[54] All samples exhibit narrow bandgaps (~2.0 eV), which enable activation under visible light irradiation, making them suitable for photocatalytic applications. Since all bandgap values fall within a narrow range of 2.0 to 2.07 eV, the differences among the samples are minor. Thus, it can be concluded that the synthesis method and crystalline phase have only a limited influence on the bandgap. All samples, regardless of synthesis method, possess bandgaps suitable for activation under visible light.

Since photocatalytic reactions occur on the surface of the photocatalyst, the specific surface area plays a crucial role in determining photocatalytic efficiency. Therefore, the textural properties and specific surface areas of the samples were measured using BET analysis. The BET surface area values are summarized in Table 4. The sample P25, prepared at room temperature, showed the lowest surface area, 3.6 (m^2 g^{-1}). Although the P25 sample shows the lowest BET surface area, the SEM images reveal that it has the smallest particle size. The reason why P25 exhibits the highest photocatalytic performance despite its lower BET surface area may be related to the limitations of the BET method in the context of wetting efficiency for liquid-phase reactions.[55] In contrast, the maximum surface area among the hydrothermal samples was 14 (m^2 g^{-1}) (H140). H160 has the lowest surface area which may be related to grain growth and larger particle size due to higher synthesis temperature. It can be concluded that for preparing the β phase, the optimum temperature is 140 °C, which provides the highest BET surface area in comparison with H120 and H160.

After determining the band gap and specific surface area of the samples to fully assess their potential for various photocatalytic processes, the complete electronic band structure was also obtained using UPS. The complete band structure of semiconductors can be estimated by determining the valence band position relative to the Fermi level and adding the optical band gap obtained from UV-vis spectroscopy to locate the conduction band. Ultraviolet photoelectron spectroscopy (UPS) was performed on P25 and H140 to assess the influence of the synthesis method and the crystal and electronic structures. The valence band edges were determined to be 1.85 eV for P25 and 1.58 eV for H140 *versus* the Fermi level using a linear approach (Fig. 7a).[56] To convert the valence and conduction band positions to the normal hydrogen electrode (NHE) scale, the work functions of the P25 and H140 samples were determined using AFM and KPFM measurements. As shown in Fig. 7(c and d), the work functions of P25 and H140 are 3.75 eV and 3.78 eV, respectively. Additional details regarding the work function measurement procedure are included in the SI.

As illustrated in Fig. 7(b), the hydrothermal synthesis of $AgVO_3$ leads to a slight downward shift in the band edges, resulting in a more negative conduction band potential. By adding the measured band gap to the valence band positions (1.13 eV for P25 and 0.92 eV for H140), the conduction band potentials for P25 and H140 were calculated to be −0.94 eV and −1.08 eV *versus* NHE, respectively. We state that these data must be taken with great care.

Table 4 Specific surface area (BET) values of the different $AgVO_3$ samples

Sample	BET surface area (m^2 g^{-1})
P25	3.61
H120	10.63
H140	14.14
H160	5.87

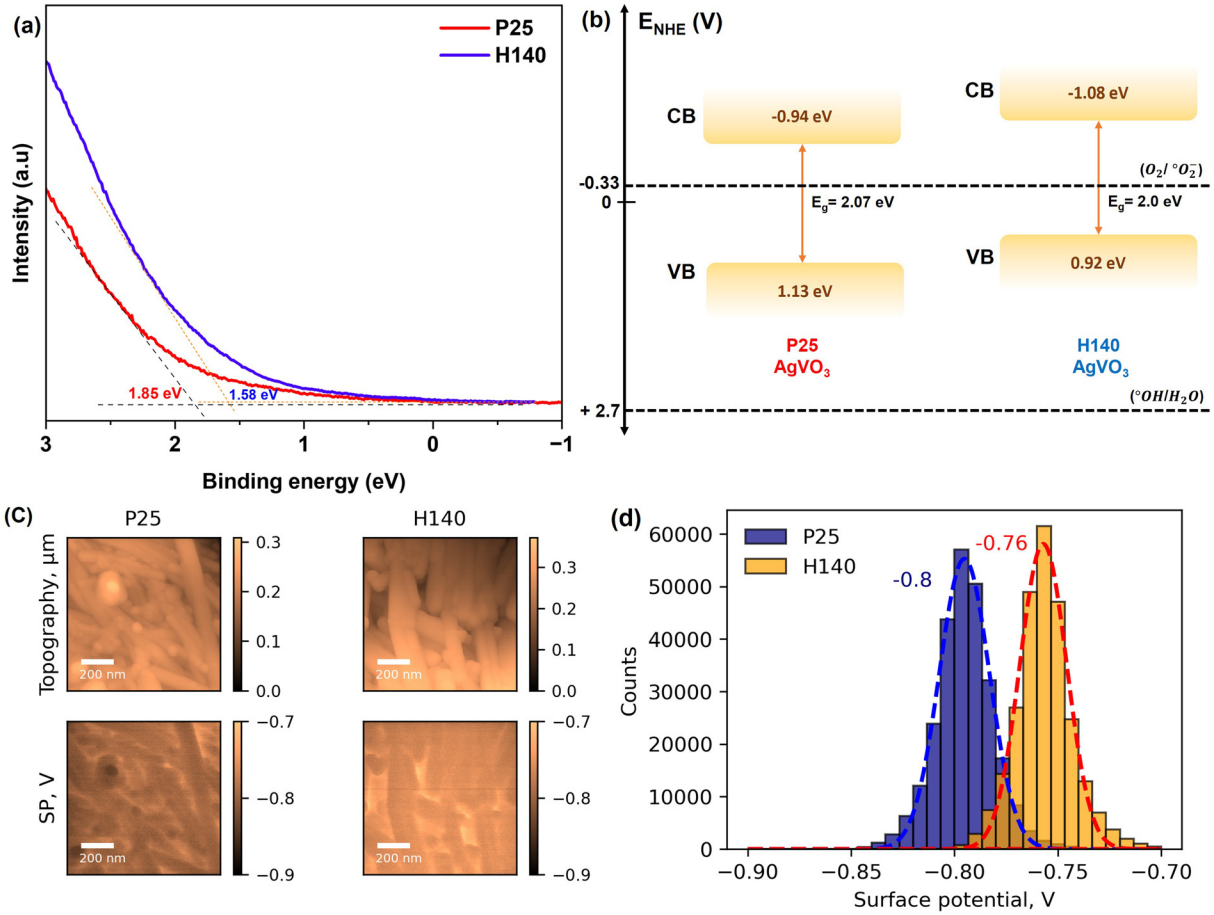

Fig. 7 (a) Valence band edge level spectra of P25 and H140 at 2100 eV ultraviolet light beam energy estimated using linear extrapolation, (b) schematic of the band structure of the $AgVO_3$ samples P25 and H140, (c) AFM and KPFM results for P25 and H140 samples, and (d) the surface potential of P25 and H140 samples.

To investigate the surface properties of the samples synthesized *via* the precipitation and hydrothermal methods, as well as the effect of the photocatalytic reaction on the surface, XPS analysis was performed on P25 and H140, and on P25 after photocatalysis. Fig. 8(a–c) show the XPS spectra of Ag, V and O for P25 and H140. In Fig. 8(a), two peaks at 368.22 and 374.22 eV correspond to Ag $3d_{5/2}$ and Ag $3d_{3/2}$, respectively. Based on the XPS and XRD results, it can be concluded that metallic silver is present on the surface of $AgVO_3$ synthesized using hydrothermal and precipitation methods. This metallic silver enhances surface conductivity and improves photocatalytic performance through the surface plasmon resonance (SPR) effect.[21] Fig. 8(b) shows high resolution XPS spectra of V 2p for the samples P25 and H140. For both samples, peaks are observed at 517.12 and 524.6 eV (517.07 and 524.55 eV for H140) corresponding to V $2p_{3/2}$ and $2p_{1/2}$, respectively, which indicate the +5 oxidation state of vanadium. Additionally, both samples display two other peaks at 517.61 and 516.55 eV (517.45 and 515.98 eV for H140) corresponding to vanadium's +4 oxidation state. In the case of oxygen, both samples show similar trends with the main peaks at 530.38 and 530.98 eV for P25 (530.17 and 530.59 eV for H140 sample), attributed to oxygen's −2 oxidation state. Moreover, a small peak at 532.95 eV is observed in the H140 sample, which is associated with hydroxyl-group formation at the surface.[57,58] These hydroxyl-groups could be formed during the high-temperature hydrothermal process at the surface of $AgVO_3$. Based on the XPS results for vanadium and oxygen, it appears that V_2O_5 and VO_2 formed which subsequently react with silver oxide to yield $AgVO_3$. Detailed XPS parameters, including peak positions, FWHM, and peak areas, are listed in Tables S1 and S2.

In addition, to further investigate the surface changes of $AgVO_3$ during the photocatalysis process, XPS analysis was performed on P25 before and after photocatalysis. The results are shown in Fig. 8(d–f). No significant differences are observed between the two states, as the main peaks for Ag, V, and O appear at the same positions. The only minor change is found in the vanadium spectra, where the peak corresponding to the +4 oxidation state shows a slight shift to higher binding energies after photocatalysis. This shift may be attributed to the oxidation of V^{4+} to V^{5+} at the surface during the photocatalysis reaction (Table S3). For all samples (P25, H140, and P25 after

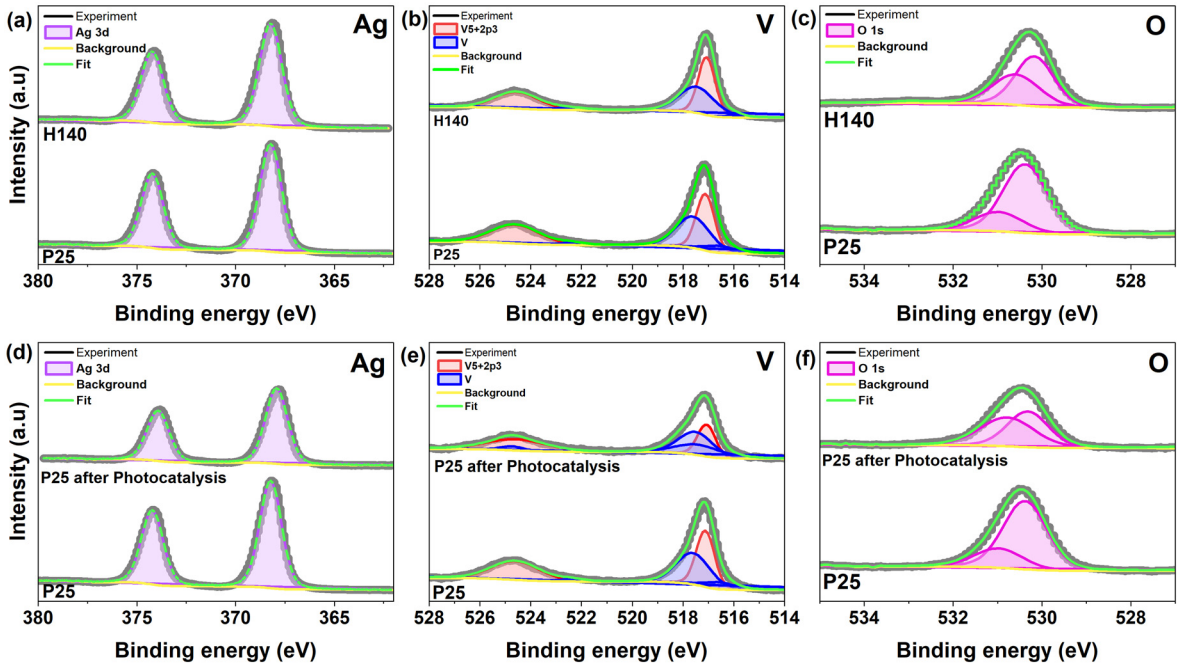

Fig. 8 XPS analysis of the $AgVO_3$ samples: (a–c) Ag, V, O scan spectra for the P25 and H140 samples and (d–f) Ag, V, O scan spectra for P25 before and after photocatalysis tests.

photocatalysis), a small carbon peak is also detected, which likely originates from surface contamination or atmospheric exposure.

3.1. Photocatalytic performance of α- and β-$AgVO_3$ for RhB degradation

To evaluate the photocatalytic performance of the synthesized samples, rhodamine B (RhB) was used as a model organic dye. Fig. 9(a–c) show the decrease in RhB concentration over time under visible light irradiation, for P25, H140 and commercial TiO_2, respectively. RhB exhibits a characteristic absorption band at 554 nm, and the decrease in intensity at this wavelength is used to monitor the degradation process. A blank test for RhB was carried out and exhibited no significant degradation after 8 hours of light irradiation in the absence of the catalyst (Fig. S1). The degradation efficiency of each sample is shown in Fig. 9(d) where P25, H120, H140 and H160 exhibit full degradation of 78%, 89% and 44%, respectively (the efficiency of samples in the present study is compared with those of previous studies in Table S4). The RhB degradation by the samples H120 and H160 are shown in Fig. S2. Overall, a good correlation is observed between the particle size and the photocatalytic performance of the samples. P25 notably exhibits the highest degradation efficiency (100% within 90 minutes) and the highest pseudo-first-order rate constant (0.061 min^{-1}). Among the hydrothermal samples, the best result achieved is 89% for H140, the enhanced RhB degradation efficiency can be attributed to its larger surface areas in comparison with the other hydrothermally prepared samples (H120, and H140). H140, H120, and H160 exhibit the surface areas: 14.14, 10.63, and 5.87 (m^2 g^{-1}), respectively, from which a correlation between the BET surface area and photocatalytic efficiency can be concluded. The exceptional performance of P25, despite its low surface area, is likely due to its morphology. The SEM images reveal that P25 consists of nanorods with an average width of 34.89 nm surrounded by larger rod-like structures. During photocatalytic degradation, the powders are stirred in an aqueous solution, reducing agglomeration and exposing more active surface area. For samples synthesized under similar conditions with comparable particle sizes, the BET results correlate well with photocatalytic performance, as observed for H120, H140, and H160.

To better evaluate the performance of the P25 sample, its photocatalytic efficiency was compared with that of commercial TiO_2 under identical experimental conditions. The TiO_2 sample achieved 99% degradation of rhodamine B after 3 hours of visible light illumination (Fig. 9c). In contrast, the P25 sample demonstrated approximately twice the efficiency, reaching complete degradation within just 90 minutes.

All samples show a hypsochromic shift in the absorption peak of RhB during degradation. The largest shift is observed for P25, where the absorption maximum shifts from 553 nm to 493 nm. Different final peak positions for P25 (493 nm) and H140 (506 nm) suggest that different degradation pathways or by-products may be involved, even though a large proportion of RhB degradation was achieved in both cases. Since RhB is degraded faster by P25 (90 min) than by H140 (89% degradation in 3 h), it is plausible that demethylation and degradation of the xanthene ring proceeds further in the P25 sample, resulting in different intermediates and final pro-

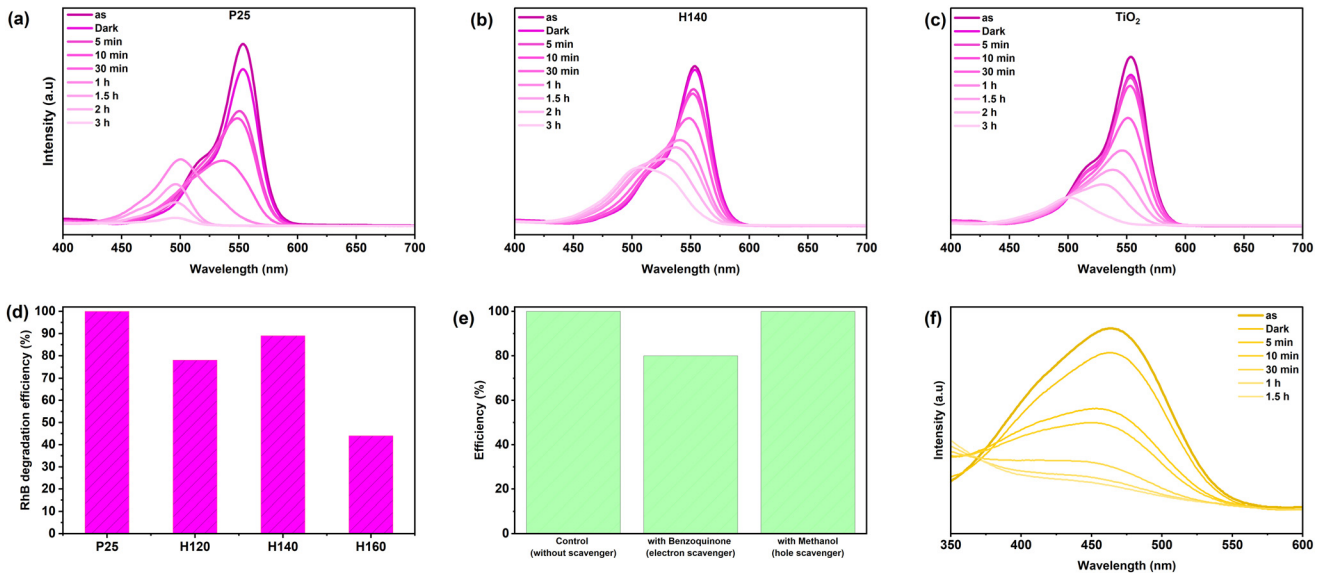

Fig. 9 UV-vis absorption spectra of rhodamine B at different time intervals under visible light irradiation using (a) P25, (b) H140, and (c) commercial TiO_2. [a–c have the same time intervals.] (d) Rhodamine B degradation efficiency using P25, H120, H140 and H160 samples, (e) efficiency of RhB removal using radical scavengers (RhB concentration: 5 mg L^{-1}, P25 dosage: 1 g L^{-1}, scavenger dosage: 1 mM), and (f) UV-vis absorption spectra of methyl orange at different time intervals under visible light irradiation using P25.

ducts.[59] Moreover, the data allow for a comparison between the α and β phases of $AgVO_3$. Previous studies have reported that the β phase generally exhibits superior photocatalytic activity due to its thermodynamic stability and reduced electron–hole recombination.[38] However, the current study presents contradictory results. The α-phase P25 shows significantly higher degradation efficiency (100%) than the β-phase samples such as H120 (78%), H140 (89%), and H160 (44%) (Fig. 9d). Based on the band structure of α and β-$AgVO_3$ (P25 and H140), electrons in the conduction band can react with oxygen to form superoxide radicals ($^{\bullet}O_2^-$) which act as reactive oxygen species (ROS) responsible for photocatalytic RhB degradation (Fig. 7b). The contribution of $^{\bullet}O_2^-$ to the degradation process was further confirmed using electron and hole scavengers. When an electron scavenger (benzoquinone) was added, the photocatalytic performance of the P25 sample decreased from 100 to 80 percent. In contrast, the addition of methanol (hole scavenger) does not significantly affect the performance of the P25 sample (Fig. 9e). It means that $^{\bullet}O_2^-$ is the primary driver of the reaction. To clarify the mechanism, electrons from the conduction band transfer to oxygen molecules, generating superoxide radicals that subsequently attack the RhB molecules and degrade their structure.[60] As shown in Fig. 7b, the conduction band of the H140 sample (−1.08 eV) is more negative than that of P25 (−0.94 eV), which may explain its lower RhB degradation kinetics.

Additionally, particle size plays an important role in photocatalytic performance. The SEM images reveal that the P25 sample has smaller particle size compared to H140 and other β-phase samples synthesized *via* hydrothermal methods. Since the β-phase samples are prepared at higher temperatures, they exhibit larger particle sizes (rods width: 61–82 nm), reducing the surface area. In contrast, the P25 sample, synthesized at room temperature, offers smaller particle size, enhancing photocatalytic activity. Therefore, the combined effect of band structure and particle size explains why the P25 sample and α-phase demonstrate superior photocatalytic performance compared to the β-phase samples.

To validate the applicability of $AgVO_3$ for anionic dyes as well, methyl orange (MO) was selected for additional testing. The optimized P25 sample was employed for the photocatalytic degradation of MO under the same conditions as RhB. The P25 sample exhibited similar performance for MO, achieving 90% removal after 90 minutes of light irradiation (Fig. 9f). These results indicate that $AgVO_3$ is capable of serving as an effective photocatalyst for both cationic (*e.g.*, RhB) and anionic (*e.g.*, MO) dye degradation.

A recyclability test was performed for the P25 sample (Fig. 10). After each cycle, the P25 sample was removed from the RhB solution and transferred to a new reactor to begin the next cycle. The results show that the P25 sample maintained its photocatalytic performance for the first three cycles; however, its efficiency decreased significantly in the subsequent cycles, dropping to approximately 50% in the fourth cycle and 25% in the fifth cycle. To investigate the cause of this decline, XRD measurements were performed after the first and fifth cycles (Fig. 10b). The results indicate that the crystal structure remained stable after the first cycle, with no noticeable changes. In contrast, after the fifth cycle, the XRD pattern revealed structural modifications, as the characteristic peaks at 12°, 17°, and 31° disappeared. This structural change explains the reduced photocatalytic efficiency observed in the later cycles.

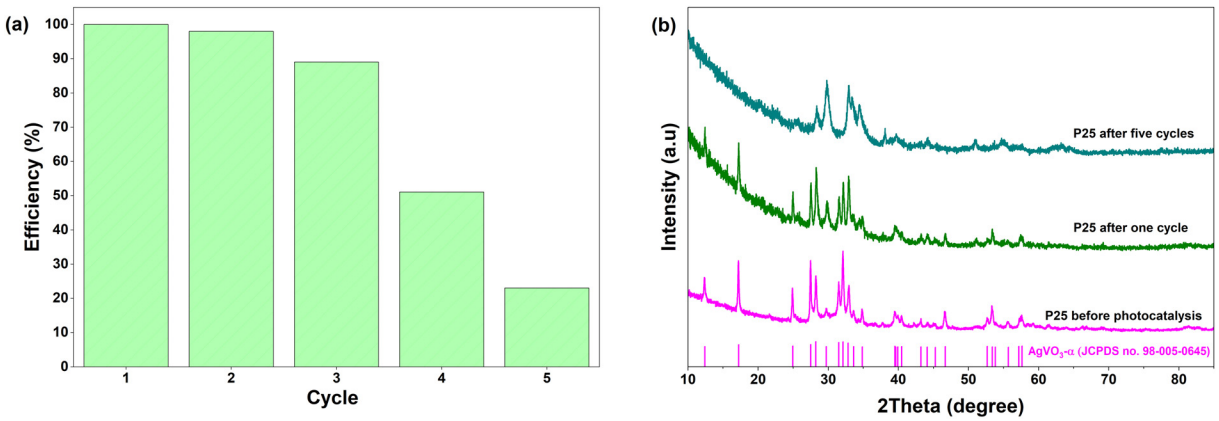

Fig. 10 (a) Photocatalytic efficiency of RhB degradation by P25 over five consecutive cycles; (b) XRD patterns of the P25 sample before photocatalysis and after the first and fifth cycles.

To gain a better understanding of the photocatalytic process and its underlying mechanism, a kinetic study was performed for all samples. Kinetic analysis is crucial for photocatalytic reactions, as these processes are highly time dependent. If the recombination rate of photogenerated charge carriers exceeds the lifetime of reactive oxygen species (ROS), such as hydroxyl radicals, the degradation reaction may not occur efficiently. Therefore, understanding the reaction kinetics is essential. Pseudo-first order, and pseudo-second order kinetic models, were employed to evaluate the photocatalytic degradation of rhodamine B (RhB), as shown in Fig. 11. The corresponding kinetic rate constants and *R*-squared values for all models are summarized in Table 5. The pseudo-first order model exhibits the best fit to the experimental data, with R^2 values ranging from 0.97 to 0.99. These values are higher compared to those for the pseudo-second order model (R^2 = 0.67–0.97). The highest pseudo-first order model rate constant was observed for the P25 sample (0.061 min^{-1}), followed by H140 (0.012 min^{-1}). In contrast, the H160 sample exhibited the lowest rate constant, which was approximately 20 times lower than that of P25.

Table 5 Kinetic rate constants and *R*-squared values for the pseudo-first order and pseudo-second order models applied to the photocatalytic degradation of rhodamine B

	Pseudo-first order model		Pseudo-second order model	
Sample	k_1 (min^{-1})	R^2	k_2 ($conc^{-1}$ min^{-1})	R^2
P25	0.061	0.97	0.760	0.67
H120	0.008	0.99	0.037	0.73
H140	0.012	0.99	0.007	0.91
H160	0.003	0.99	0.001	0.97

After comparing the photocatalytic performance of α- and β-$AgVO_3$ samples, it is concluded that the P25 sample with the α-phase structure exhibits higher efficiency than the β-phase samples. To further optimize its performance, the effects of

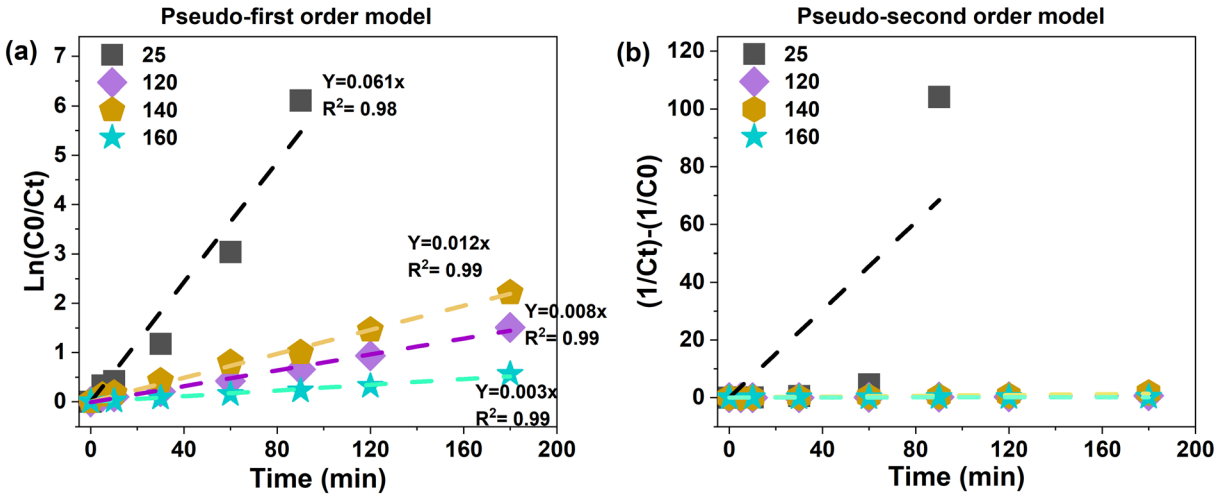

Fig. 11 Kinetic analysis of RhB degradation using (a) pseudo-first order and (b) pseudo-second order models for all synthesized samples.

pH and catalyst dosage were investigated (Fig. S4 and S5). The results indicate that the sample performs better in basic solutions compared to acidic ones. The pH of the RhB solution after adding the P25 sample was 5.5, which was used as the control sample. A more acidic environment reduces the photocatalytic activity, whereas under basic conditions the sample maintains its performance. Additionally, increasing the catalyst dosage beyond 0.75 g L^{-1} leads to complete RhB degradation. At 0.75 g L^{-1}, full dye degradation occurs after 180 minutes, while at 1 g L^{-1} complete degradation is achieved within 90 minutes. Therefore, 1 g L^{-1} is identified as the optimum $AgVO_3$ dosage for RhB degradation.

4. Conclusion

In this study, facile, repeatable synthesis routes for producing both α- and β-phases of $AgVO_3$ were successfully developed. The metastable α-phase was synthesized *via* a simple precipitation method at room temperature, while the formation of the thermodynamically stable β-phase required hydrothermal synthesis at elevated temperatures (120–160 °C). Notably, the β-phase could not be obtained through the precipitation method. Although both α- and β-$AgVO_3$ crystallize in a monoclinic system, they differ in space group symmetry: the α-phase adopts the $C2/c$ space group, whereas the β-phase crystallizes in the $C2/m$ space group. All samples display rod-like morphologies; however, the α-phase (P25) exhibits a distinctive tree-like architecture, characterized by nanorod growth on microrods. Differential scanning calorimetry (DSC), complemented by high-temperature X-ray diffraction and calcination studies, confirmed an irreversible α → β phase transition occurring between ~200 and 240 °C. All samples exhibit small optical bandgaps (~2.0 eV), enabling visible-light-driven photocatalysis. The full electronic band structures of α- and β-$AgVO_3$ were determined, with their conduction and valence band positions calculated to be (−0.94 eV, 1.13 eV) and (−1.08 eV, 0.92 eV) *versus* NHE, respectively.

In contrast to previous studies that favor the β-phase for photocatalysis, the α-phase demonstrates significantly higher photocatalytic performance. The P25 sample achieved complete rhodamine B degradation within 90 minutes, while the best-performing β-phase sample reached only 89% after 180 minutes. This highlights the crucial influence of morphology and surface characteristics over crystallinity in determining photocatalytic efficiency. Kinetic analysis revealed that the RhB degradation follows a pseudo-first-order model, with the highest rate constant observed for the P25 sample to be 0.061 min^{-1}.

Author contributions

H. E.: investigation, visualization, formal analysis, methodology, data curation, and writing – original draft. M. E. C.: data curation, formal analysis, and writing – review & editing. A. D.: conceptualization, supervision, literature survey, data curation, formal analysis, and writing – review & editing. Y. U. J.: investigation and formal analysis. S. M. F.: investigation and formal analysis. C. O.: resources. E. T.: investigation. S. T.: investigation. D. C. L.: supervision, project administration, and funding acquisition.

Conflicts of interest

There are no conflicts to declare.

Data availability

The data that support the findings of this study are available from the corresponding authors upon reasonable request.

Supplementary information (SI) is available. See DOI: https://doi.org/10.1039/d5nr04142b.

Acknowledgements

H. Esmaili wishes to thank the financial support from the German Academic Exchange Service (DAAD) for this project. A. Dubey acknowledges the PRIME postdoctoral funding.

The authors also thank Prof. Matthias Epple's research group for FTIR measurements and Dr Ulrich Hagemann for XPS and UPS measurements. Prof. Niels Benson, Witchaya Arpavate, Lars Leander Schaberg, Amirhosein Paryab and Dr Boris Slautin are acknowledged for their scientific discussions.

References

1 V. Katheresan, J. Kansedo and S. Y. Lau, *J. Environ. Chem. Eng.*, 2018, **6**, 4676–4697.
2 T. Bavani, J. Madhavan, S. Prasad, M. S. AlSalhi, M. Aljaffreh and S. Vijayanand, *Environ. Res.*, 2021, **200**, 111365.
3 H. Wang, X. Liu, P. Niu, S. Wang, J. Shi and L. Li, *Matter*, 2020, **2**, 1377–1413.
4 C. Karthikeyan, P. Arunachalam, K. Ramachandran, A. M. Al-Mayouf and S. Karuppuchamy, *J. Alloys Compd.*, 2020, **828**, 154281.
5 S. Zhang, X. Ou, Q. Xiang, S. A. Carabineiro, J. Fan and K. Lv, *Chemosphere*, 2022, **303**, 135085.
6 A. Kumar, A. Kumar and V. Krishnan, *ACS Catal.*, 2020, **10**, 10253–10315.
7 I. Ahmad, G. Li, A. Al-Qattan, A. J. Obaidullah, A. Mahal, M. Duan, K. Ali, Y. Y. Ghadi and I. Ali, *Mater. Today Sustain.*, 2024, **25**, 100666.
8 H. L. Tan, R. Amal and Y. H. Ng, *J. Mater. Chem. A*, 2017, **5**, 16498–16521.
9 R. Konta, H. Kato, H. Kobayashi and A. Kudo, *Phys. Chem. Chem. Phys.*, 2003, **5**, 3061–3065.
10 R. Yang, Y. Zhang, Y. Fan, R. Wang, R. Zhu, Y. Tang, Z. Yin and Z. Zeng, *Chem. Eng. J.*, 2022, **428**, 131145.

11 H. Chen, J. Zeng, M. Chen, Z. Chen, M. Ji, J. Zhao, J. Xia and H. Li, *Chin. J. Catal.*, 2019, **40**, 744–754.
12 R. Yang, Z. Zhu, C. Hu, S. Zhong, L. Zhang, B. Liu and W. Wang, *Chem. Eng. J.*, 2020, **390**, 124522.
13 Y. Chen, Y. Zhang, W. Wang, X. Xu, Y. Li, M. Du, Z. Li and Z. Zou, *Sol. RRL*, 2022, **6**, 2200099.
14 A. Bafaqeer, M. Tahir and N. A. S. Amin, *Appl. Surf. Sci.*, 2018, **435**, 953–962.
15 N. K. Veldurthi, N. K. Eswar, S. A. Singh and G. Madras, *Appl. Catal., B*, 2018, **220**, 512–523.
16 Q. A. Alsulami, A. Rajeh, M. A. Mannaa, S. M. Albukhari and D. F. Baamer, *Int. J. Hydrogen Energy*, 2021, **46**, 27349–27363.
17 M. Gunawan, M. Priest, D. Gunawan, S. Nie, A. Satriyatama, J. Vongsvivut, Z. Hameiri, Q. Zhang, S. Zhou and R. Amal, *Energy Environ. Sustain.*, 2025, **1**, 100019.
18 H. Dong, G. Chen, J. Sun, Y. Feng, C. Li and C. Lv, *Chem. Commun.*, 2014, **50**, 6596–6599.
19 P. Ju, H. Fan, B. Zhang, K. Shang, T. Liu, S. Ai and D. Zhang, *Sep. Purif. Technol.*, 2013, **109**, 107–110.
20 T. Bavani, J. Madhavan, S. Prasad, M. S. AlSalhi and M. J. AlJaafreh, *Environ. Pollut.*, 2021, **269**, 116067.
21 Z. Liu, Y. Liu, X. Sun, H. Ji, W. Liu and Z. Cai, *Chem. Eng. J.*, 2022, **433**, 133604.
22 K. K. Mandari, N. Son, T. Kim and M. Kang, *J. Alloys Compd.*, 2022, **927**, 166886.
23 S. Bera, S. Ghosh and R. N. Basu, *J. Alloys Compd.*, 2020, **830**, 154527.
24 Q. Wang, X. Zhou, S. Ji, S. Li, J. Gu, L. Shen, P. Liu, J. Yin, G. Xu and W. Shi, *J. Environ. Chem. Eng.*, 2021, **9**, 106498.
25 H. Shi, C. Zhou and C. Zhang, *Res. Chem. Intermed.*, 2015, **41**, 7725–7737.
26 V. Sivakumar, R. Suresh, K. Giribabu and V. Narayanan, *Solid State Sci.*, 2015, **39**, 34–39.
27 W. Klockner, R. Yadav, J. Yao, S. Lei, A. Aliyan, J. Wu, A. Martí, R. Vajtai, P. Ajayan and J. Denardin, *J. Nanopart. Res.*, 2017, **19**, 1–14.
28 R. C. Oliveira, M. M. Teixeira, J. P. C. Costa, M. Penha, E. M. Francisco, J. S. da Silva, M. S. Li, E. Longo, L. Gracia and J. Andres, *Ceram. Int.*, 2018, **44**, 5939–5944.
29 R. D. Holtz, B. A. Lima, A. G. Souza Filho, M. Brocchi and O. L. Alves, *Nanomedicine*, 2012, **8**, 935–940.
30 A. P. de Melo Monteiro, R. Dias Holtz, L. Carneiro Fonseca, C. H. Zanini Martins, M. de Sousa, L. A. V. de Luna, D. L. de Sousa Maia and O. L. Alves, *Chem. Rec.*, 2018, **18**, 973–985.
31 K. Momma and F. Izumi, *Appl. Crystallogr.*, 2008, **41**, 653–658.
32 P. Rozier, J.-M. Savariault and J. Galy, *J. Solid State Chem.*, 1996, **122**, 303–308.
33 S. Kittaka, K. Matsuno and H. Akashi, *J. Solid State Chem.*, 1999, **142**, 360–367.
34 M. K. Horton, P. Huck, R. X. Yang, J. M. Munro, S. Dwaraknath, A. M. Ganose, R. S. Kingsbury, M. Wen, J. X. Shen and T. S. Mathis, *Nat. Mater.*, 2025, 1–11.
35 H. Zeng, Q. Wang and Y. Rao, *RSC Adv.*, 2015, **5**, 3011–3015.
36 J. Guo, J. Liang, X. Yuan, L. Jiang, G. Zeng, H. Yu and J. Zhang, *Chem. Eng. J.*, 2018, **352**, 782–802.
37 D. McNulty, Q. Ramasse and C. O'Dwyer, *Nanoscale*, 2016, **8**, 16266–16275.
38 M. Pudukudy, Q. Jia, H. Wang, S. Shan and R. Rajendran, *Mater. Sci. Semicond. Process.*, 2020, **107**, 104824.
39 B. D. Cullity and R. Smoluchowski, *Phys. Today*, 1957, **10**, 50–50.
40 H. Zhang, X. Lv, Y. Li, Y. Wang and J. Li, *ACS Nano*, 2010, **4**, 380–386.
41 W. Gao, C. Ran, M. Wang, L. Li, Z. Sun and X. Yao, *Phys. Chem. Chem. Phys.*, 2016, **18**, 18219–18226.
42 Y. Zhu, Y. Wang, W. Yao, R. Zong and Y. Zhu, *RSC Adv.*, 2015, **5**, 29201–29208.
43 A. W. Mureithi, Y. Sun, T. Mani, A. R. Howell and J. Zhao, *Cell Rep. Phys. Sci.*, 2022, **3**, 1–14.
44 M. A. Henderson and M. Shen, *Top. Catal.*, 2017, **60**, 440–445.
45 H. D. Tran, D. Q. Nguyen, P. T. Do and U. N. Tran, *RSC Adv.*, 2023, **13**, 16915–16925.
46 B. R. C. de Menezes, R. G. Ribas, V. M. Schatkoski, T. L. do Amaral Montanheiro, C. Y. Koga-Ito and G. P. Thim, *SN Appl. Sci.*, 2019, **1**, 1327.
47 H. Ahmad, A. B. Siddique, S. Zaheer, R. Sattar, A. Abbas, M. Amin, R. Al-Salahi, H. A. Abuelizz and M. Z. Saleem, *J. Water Process Eng.*, 2025, **74**, 107855.
48 H. Esmaili, S. Sheibani and F. Rashchi, *Particuology*, 2018, **37**, 72–80.
49 R. L. Frost, S. J. Palmer, J. Čejka, J. Sejkora, J. Plášil, S. Bahfenne and E. C. Keeffe, *J. Raman Spectrosc.*, 2011, **42**, 1701–1710.
50 H. H. Ibrahim, A. Abdelghany, M. H. Gaber and S. A. Ali, *Opt. Quantum Electron.*, 2024, **56**, 435.
51 M. S. Mansha and T. Iqbal, *Opt. Mater.*, 2022, **131**, 112591.
52 P. Makuła, M. Pacia and W. Macyk, *J. Phys. Chem. Lett.*, 2018, **9**, 6814–6817.
53 W. Zhao, Y. Guo, Y. Faiz, W.-T. Yuan, C. Sun, S.-M. Wang, Y.-H. Deng, Y. Zhuang, Y. Li and X.-M. Wang, *Appl. Catal., B*, 2015, **163**, 288–297.
54 A. Beltran, L. Gracia, J. Andres and E. Longo, *J. Phys. Chem. C*, 2017, **121**, 27624–27642.
55 T. L. Hill, in *Advances in catalysis*, Elsevier, 1952, vol. 4, pp. 211–258.
56 B. Philippe, T. J. Jacobsson, J.-P. Correa-Baena, N. K. Jena, A. Banerjee, S. Chakraborty, U. B. Cappel, R. Ahuja, A. Hagfeldt and M. Odelius, *J. Phys. Chem. C*, 2017, **121**, 26655–26666.
57 E. McCafferty and J. Wightman, *Surf. Interface Anal.*, 1998, **26**, 549–564.
58 G. P. López, D. G. Castner and B. D. Ratner, *Surf. Interface Anal.*, 1991, **17**, 267–272.
59 H. Fu, S. Zhang, T. Xu, Y. Zhu and J. Chen, *Environ. Sci. Technol.*, 2008, **42**, 2085–2091.
60 A. B. Siddique, M. A. Shaheen, A. Abbas, Y. Zaman, H. M. Amin, M. M. Alam, N. K. Alharbi, F. Alshehri, A. Shami and F. A. Al-Joufi, *Int. J. Environ. Anal. Chem.*, 2025, 1–23.